level spacing in Xe atoms and Xe ions. It is therefore quite likely that a quantum mechanical description of the absorption process which includes resonant intermediate states could give larger absorption than the classical model.

In conclusion, absorption of short-wavelength radiation and subsequent ionization in clusters differs considerably from that in the optical spectral range. Absorption and ionization start by single-photon absorption as described by quantum mechanics. After many unbound electrons are created, a plasma is formed. Our experimental results give evidence that absorption in such cluster plasma is stronger than predicted by calculations with classical models. We assume that quantum-mechanical modelling is needed at these short wavelengths to explain the efficient energy deposition seen in the experiment. On the other hand, the classical simulation clearly shows that electrons can leave the cluster by a photon-assisted thermionic emission. Field ionization, the dominant ionization process at optical frequencies, does not contribute to cluster ionization.   □

1. Batani, D., Joachain, C. J., Martellucci, S. & Chester, A. N. *Atoms, Solids, and Plasmas in Super-Intense Laser Fields* (Kluwer Academic, New York, 2001).
2. Smith, R. & Key, M. H. *X-Ray Lasers 2000* (eds Jamelot, L. G., Möller, C. & Klinsnick, A.) 383–388 (EDP Science, Saint Malo, 2000).
3. Andruszkow, J. *et al.* First observation of self-amplified spontaneous emission in a free-electron laser at 109 nm wavelength. *Phys. Rev. Lett.* **85**, 3825–3828 (2000).
4. Ayvazyan, V. *et al.* Generation of GW radiation pulses from a VUV free-electron laser operating in the femtosecond regime. *Phys. Rev. Lett.* **88**, 104802 (2002).
5. Åberg, T., *et al.* DESY Report TESLA FEL 95-03 (DESY, Hamburg, 1995).
6. Materlik, G. & Tschentscher, T. (eds) *DESY Report TESLA FEL 2001-05* (DESY, Hamburg, 2001).
7. Shenoy, G. K. & Stöhr, J. *LCLS: The First Experiments* (SLAC, Stanford, 2000).
8. Neutze, R., Wouts, R., van der Spoel, D., Weckert, E. & Haidu, J. Potential for biomolecular imaging with femtoscond X-ray pulses. *Nature* **406**, 752–757 (2000).
9. Russek, M., Lagadec, H. & Blenski, T. Cluster explosion in an intense laser pulse: Thomas-Fermi model. *Phys. Rev. A* **63**, 13203 (2000).
10. Synder, E. M., Buzza, S. A. & Castleman, A. W. Jr Intense field matter interactions: Multiple ionisation of clusters. *Phys. Rev. Lett.* **77**, 3347–3350 (1996).
11. Ditmire, T. *et al.* High-energy ions produced in explosions of superheated atomic clusters. *Nature* **386**, 54–56 (1997).
12. Ditmire, T., Donnelly, T., Rubenchik, A. M., Falcone, R. W. & Perry, M. D. Interaction of intense pulses with atomic clusters. *Phys. Rev. A* **53**, 3379–3402 (1996).
13. Lezius, M., Dobosz, S., Normand, D. & Schmidt, M. Explosion dynamics of rare gas clusters in strong laser fields. *Phys. Rev. Lett.* **80**, 261–264 (1998).
14. Köller, L. *et al.* Plasmon-enhanced multi-ionization of small metal clusters in strong femtosecond laser fields. *Phys. Rev. Lett.* **82**, 3783–3786 (1999).
15. Shao, Y. L. *et al.* Multi-keV electron generation in the interaction of intense laser pulses with Xe clusters. *Phys. Rev. Lett.* **77**, 3343–3346 (1996).
16. Rose-Petruck, C., Schafer, K. J., Wilson, K. R. & Barty, C. P. J. Ultrafast electron dynamics and inner-shell ionization in laser driven clusters. *Phys. Rev. A* **55**, 1182–1190 (1996).
17. Last, I. & Jortner, J. Quasiresonance ionization of large multicharged clusters in a strong laser field. *Phys. Rev. A* **60**, 2215–2221 (1999).
18. Last, I. & Jortner, J. Dynamics of Coulomb explosion of large clusters in a strong laser field. *Phys. Rev. A* **62**, 13201 (2000).
19. Brewczyk, M., Clark, C. W., Lewenstein, M. & Rzazewski, K. Stepwise explosion of atomic clusters induced by a strong laser field. *Phys. Rev. Lett.* **80**, 1857–1860 (1998).
20. Krainov, V. P. & Roshchupin, A. S. Dynamics of Coulomb explosion of large Xe clusters irradiated by a super-intense ultra-short laser pulse. *J. Phys. B* **34**, L297–L303 (2001).
21. McPherson, A., Thompson, B. D., Borisov, A. B., Boyer, K. & Rhodes, C. K. Multiphoton-induced X-ray emission at 4-5 keV from Xe atoms with multiple core vacancies. *Nature* **370**, 631–634 (1994).
22. Brewczyk, M. & Rzazewski, K. Over-the-barrier ionization of multi electron atoms by intense VUV free-electron laser. *J. Phys. B* **32**, L1–L4 (1999).
23. Delone, N. B. & Krainov, V. P. *Multiphoton Process in Atoms* (ed. Lambropoulos, P.) 1–3 (Springer, Berlin, 2000).
24. Samson, J. A. R. New energy levels in xenon and krypton. *Phys. Lett.* **8**, 107–108 (1964).
25. Aust, S., Strickland, D., Meyerhofer, D. D., Chin, S. L. & Eberly, J. H. Tunneling ionization of noble gases in a high-intensity laser field. *Phys. Rev. Lett.* **63**, 2212–2215 (1989).
26. Brunel, F. Not-so resonant, resonant absorption. *Phys. Rev. Lett.* **59**, 52–55 (1987).
27. Kostyukov, I. Y. Inverse-bremsstrahlung absorption of an intense laser field in cluster plasma. *JETP Lett.* **73**, 393–397 (2001).
28. Hagena, O. F. Condensation in free jets: Comparison of rare gases and metals. *Z. Phys. D* **4**, 291–299 (1987).
29. Karnbach, R., Joppien, M., Stapelfeldt, J., Wörmer, J. & Möller, T. CLULU: An experimental setup for luminescence measurements on van der Waals clusters with synchrotron radiation. *Rev. Sci. Instrum.* **64**, 2838–2849 (1993).

....

Non-framework cation migration and irreversible pressure-induced hydration in a zeolite

Yongjae Lee*, Thomas Vogt*, Joseph A. Hriljac†, John B. Parise‡, Jonathan C. Hanson§ & Sun Jin Kim‖

* *Physics Department, Brookhaven National Laboratory, Upton, New York 11973, USA*
† *School of Chemical Sciences, University of Birmingham, Birmingham B15 2TT, UK*
‡ *Geosciences Department, State University of New York, Stony Brook, New York 11794, USA*
§ *Chemistry Department, Brookhaven National Laboratory, Upton, New York 11973, USA*
‖ *Nano-Materials Research Center, Korea Institute of Science and Technology, Seoul 130-650, Korea*

....

Zeolites crystallize in a variety of three-dimensional structures in which oxygen atoms are shared between tetrahedra containing silicon and/or aluminium, thus yielding negatively charged tetrahedral frameworks that enclose cavities and pores of molecular dimensions occupied by charge-balancing metal cations and water molecules[1]. Cation migration in the pores and changes in water content associated with concomitant relaxation of the framework have been observed in numerous variable-temperature studies[2–5], whereas the effects of hydrostatic pressure on the structure and properties of zeolites are less well explored[6–8]. The zeolite sodium aluminosilicate natrolite was recently shown to undergo a volume expansion at pressures above 1.2 GPa as a result of reversible pressure-induced hydration[9]; in contrast, a synthetic analogue, potassium gallosilicate natrolite, exhibited irreversible pressure-induced hydration with retention of the high-pressure phase at ambient conditions[10]. Here we report the structure of the high-pressure recovered phase and contrast it with the high-pressure phase of the sodium aluminosilicate natrolite. Our findings show that the irreversible hydration behaviour is associated with a pronounced rearrangement of the non-framework metal ions, thus emphasizing that they can clearly have an important role in mediating the overall properties of zeolites.

The pressure-induced changes of the unit cell parameters of a powder sample of the potassium gallosilicate form of natrolite (K-GaSi-NAT) reveal a volume expansion of about 1.0% between 1.2(1) and 1.7(1) GPa (numbers in parentheses are errors on measured pressures) (Fig. 1a)[10]. Structurally, this expansion differs from that observed in the sodium aluminosilicate form of natrolite (Na-AlSi-NAT): in K-GaSi-NAT, the *c*-axis, along which the rigid T_5O_{10} (T = Al, Si, Ga, and so on) tetrahedral building units join to form a chain (Fig. 1b), expands by about 0.4%, whereas it
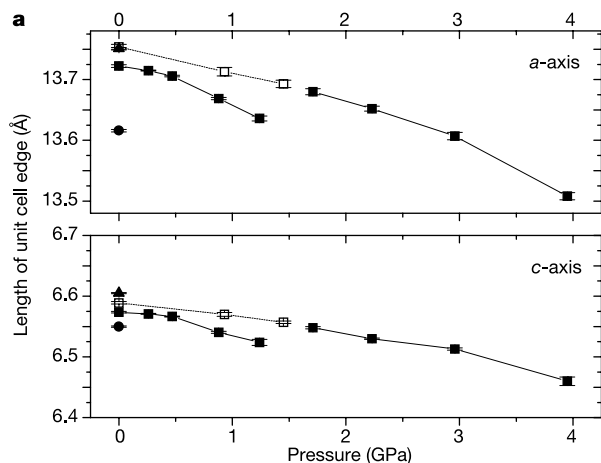
Figure 1 Structural features of the natrolite framework and its pressure response. **a**, Evolution of the unit-cell edge lengths (Å) with pressure for K-GaSi-NAT. Squares represent increase (filled) and release (unfilled) of pressure from the *in situ* measurements. Triangles and circles indicate measurements at room temperature and −160 °C, respectively, on a single crystal recovered from 1.9 GPa. **b**, A polyhedral representation of the chain found in the NAT framework shown along [010] (left) and [001] (upper right). The repeat distance of the T_5O_{10} building unit of five Ga/Si- (or Al/Si-) tetrahedra constitutes the *c*-axis length (*c*). Lower right, a simplified skeletal
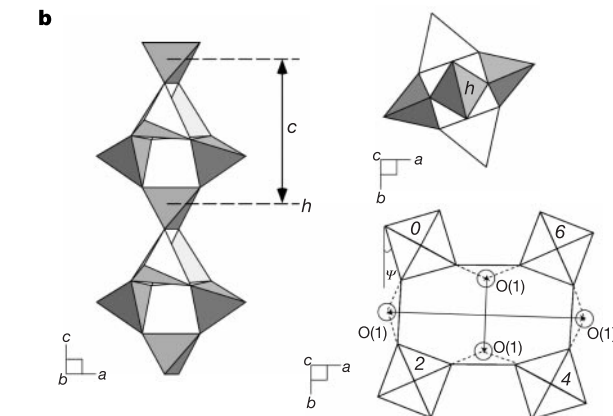
representation of the channel along the *c*-axis. The height (*h*) of the central tetrahedral node (upper right) can be described in terms of eighths of the repeat distance, and natrolite shows a *2460*-type connectivity of the neighbouring chains. Vertices represent Ga/Si- (or Al/Si-) tetrahedral atoms, and oxygen atoms are omitted. The overall rotation angle of the chains, ψ, is defined by the (average) angle between the sides of the quadrilateral around the chain and the *a*- (and *b*-) axis. The O(1) oxygen atoms are shown to permit visualization of the channel openings in the GaSi-NAT framework.

contracts continuously in Na-AlSi-NAT (ref. 9). The pressure-induced expansion in K-GaSi-NAT is therefore three-dimensional, but is essentially two-dimensional in Na-AlSi-NAT. More strikingly, the larger-volume phase of K-GaSi-NAT endures after pressure release at ambient conditions (Fig. 1a), with the unit cell volume of the recovered sample being 0.8% larger (more than 40σ) than that

measured before compression. Diffraction data were collected 3 and 8 days after pressure release and, within 5σ, no indication of a further volume contraction was detected.

Because the powder form of the high-pressure phase of K-GaSi-NAT can be retained at ambient conditions, a successful attempt was made to produce single crystals (see Methods). The structure was
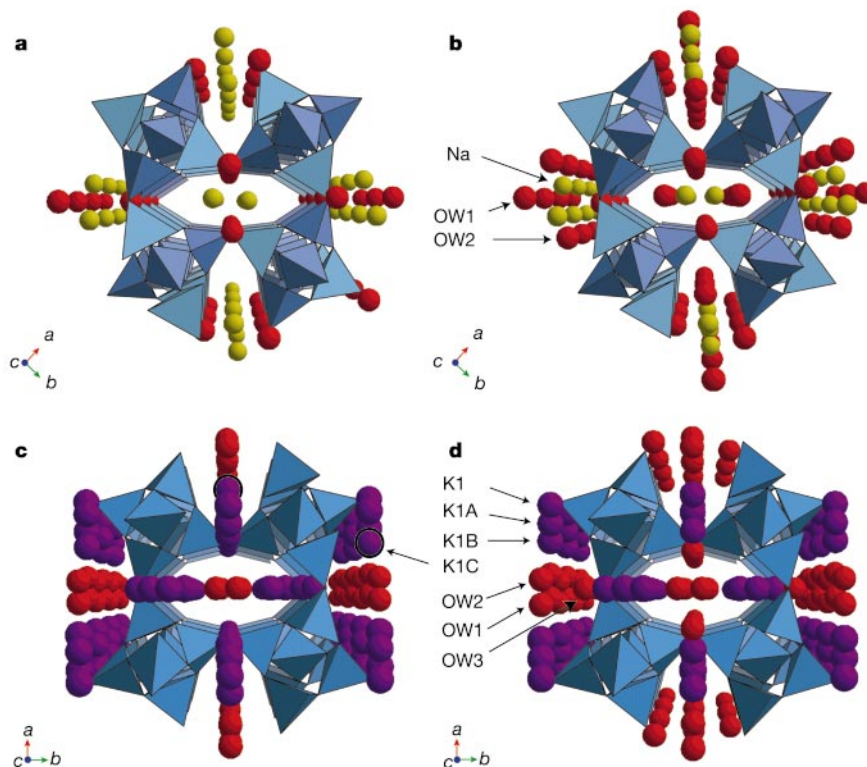

Figure 2 Polyhedral representations of Na-AlSi-NAT and K-GaSi-NAT before and after pressure-induced hydration. **a**, Na-AlSi-NAT at 0.40 GPa; **b**, Na-AlSi-NAT at 1.51 GPa; **c**, K-GaSi-NAT as synthesized; **d**, K-GaSi-NAT recovered from 1.9 GPa. Tetrahedra in

Na-AlSi-NAT are shown in two colours to illustrate the ordering of Al/Si over the framework tetrahedral sites, whereas Ga/Si in K-GaSi-NAT are disordered and shown in one colour. K1C atoms are emphasized with bold outlines (see the text).

determined *ex situ*, and the crystal structures of K-GaSi-NAT before and after pressure-induced hydration (PIH) are shown in Fig. 2 and compared with the structures of Na-AlSi-NAT from an *in situ* pressure experiment[9,10]. The water contents of both K-GaSi-NAT and Na-AlSi-NAT double after PIH; for K-GaSi-NAT the refined unit-cell compositions before and after the pressure experiment are $K_{7.5(3)}Ga_{8.0(1)}Si_{12.0(1)}O_{40}\cdot6.3(6)H_2O$ and $K_{7.9(5)}Ga_8Si_{12}O_{40}\cdot12.24(16)H_2O$, respectively (Supplementary Table 1). After PIH, a new partly occupied water site OW3 appears in close proximity to the statistically distributed potassium cation sites. This causes the potassium cations, distributed over K1, K1A, K1B and K1C sites, to migrate away from the centre of the channel and merge into three sites. The occupancies of the initial water sites OW1 and OW2 increase by 64% and 35%, respectively. All water molecules, including those located at the new OW3 site, coordinate to the potassium cations, with interatomic distances ranging from 2.45(12) to 3.35(13) Å (Supplementary Table 2). As a consequence, the average

potassium-to-framework oxygen distance range increases from 2.661(4)–2.794(9) Å to 2.71(1)–2.92(2) Å. The pressure-induced expansion is thus related to an overbonding of the potassium cations.

Another structural response during PIH is the decrease in the overall rotation angle of the chains, ψ, from $17.5(1)°$ to $17.0(1)°$ (see Fig. 1b). This change in ψ with pressure is similar to, although smaller than, the corresponding change observed in Na-AlSi-NAT and suggests that PIH is coupled to the relaxation of the overall framework distortion by expanding the pore space across the channel; in fact, the opening of the channel, defined by the shortest and longest interatomic distances between two chain-bridging oxygens (O(1); see Fig. 1b), increases from $5.70(1)$ Å $\times$ $9.54(1)$ Å to $5.80(1)$ Å $\times$ $9.57(1)$ Å before and after PIH, respectively. However, the degree of overall chain rotation is much less than those observed in the aluminosilicate natrolite ($23.7(1)°$ to $26.4(1)°$). The reason for this is attributed to a combined effect of the different non-framework cation distributions and the increased flexibility of
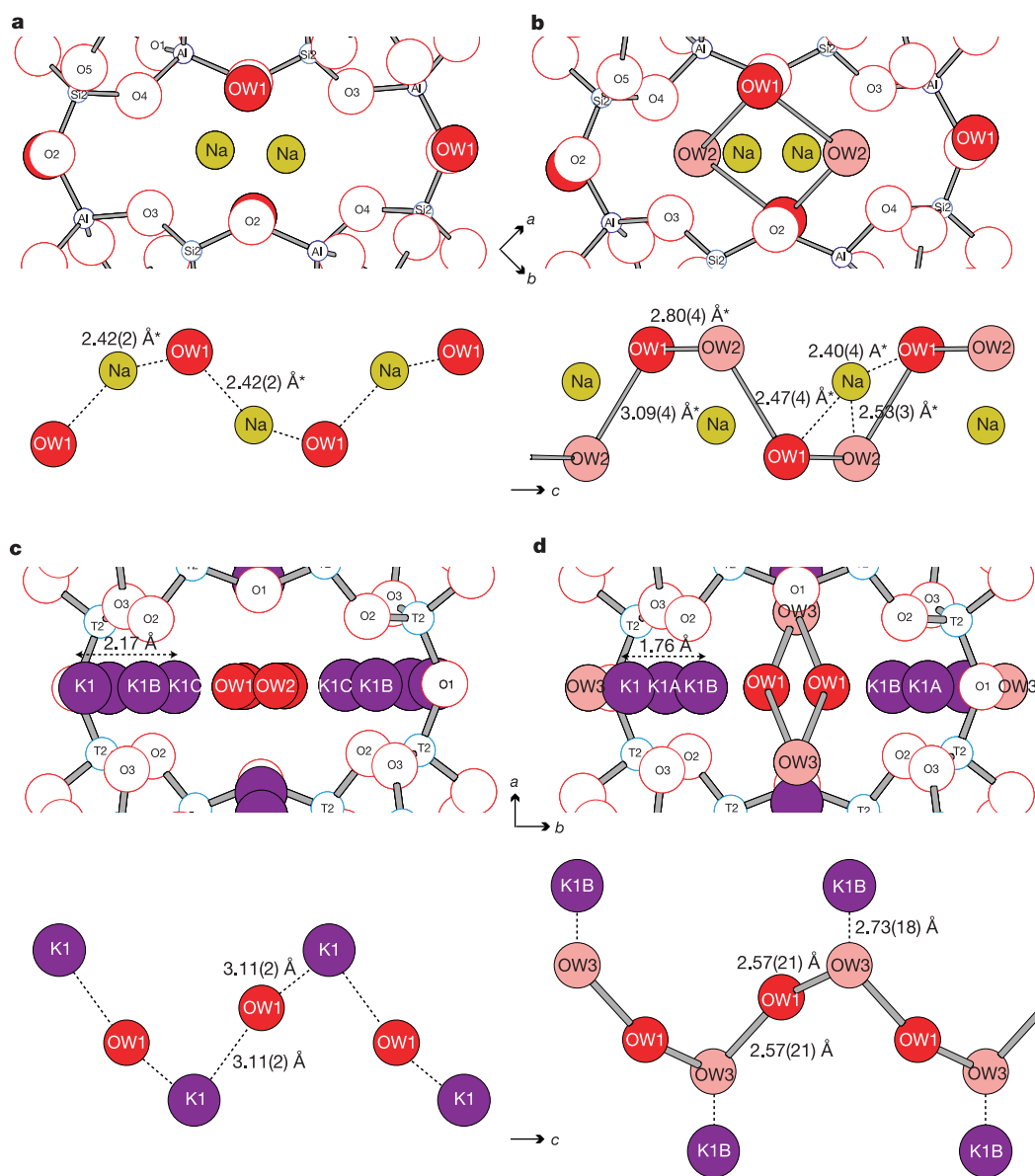

Figure 3 Expanded views of the channel contents of Na-AlSi-NAT and K-GaSi-NAT before and after pressure-induced hydration. **a**, Na-AlSi-NAT at 0.40 GPa; **b**, Na-AlSi-NAT at 1.51 GPa; **c**, K-GaSi-NAT as synthesized; **d**, K-GaSi-NAT recovered from 1.9 GPa. Each lower figure shows a view perpendicular to the channel axis. Hydrogen bondings of water nanostructures (**b** and **d**) are emphasized with thick lines, and interactions between water and non-framework cations are shown with dotted lines. New water sites are emphasized in light red. For K-GaSi-NAT, the water molecules at the statistical OW2 site are not shown for clarity (lower **c** and **d**) and one of the potassium sites is chosen to emphasize the cation migration (lower **c** and lower **d**). Structural details of Na-AlSi-NAT were taken from ref. 10.

the T–O–T angles in K-GaSi-NAT than in Na-AlSi-NAT. The latter might also explain the three-dimensional swelling unique to the gallosilicate natrolite in contrast to the two-dimensional swelling of Na-AlSi-NAT. Given the greater flexibility of the T–O–T angle in the gallosilicate framework, the incorporation of additional water molecules into the channels at high pressure would allow the T–O–T angles within the chain (T–O(2)–T and T–O(3)–T) to relax together with the angles between the chains (T–O(1)–T; see Fig. 1b and Supplementary Table 2).

In an attempt to decrease the static crystallographic disorder of the non-framework species in the PIH state of K-GaSi-NAT as well as to explore the reversibility back to the original state, variable-temperature experiments were performed with the same quenched single crystal. The cell parameters measured at room temperature (24 °C) after 1 month at ambient conditions did not show any changes (within 2σ) from the values measured immediately after the pressure release, confirming again the long-term retention of pressure-induced hydration at ambient conditions. The temperature was then decreased to −160 °C with a stream of dry N_2 blowing onto the crystal. However, it was found that under these conditions the material lost its excess water, vacating the OW3 site, and the potassium cations shifted back towards the vacant water site away from the channel walls (Supplementary Table 1). The occupancy of the K1 site was 40% less than in the original state before PIH, and the K1C site was not reoccupied when losing the excess water. This shows that the potassium redistribution was not completely reversible even when the PIH was reversed. As the temperature was increased to room temperature (24 °C) again, an unknown small-volume phase formed. This new phase persisted after heating to 100 °C. Work is in progress to investigate in greater detail the structural evolutions of both phases of K-GaSi-NAT as a function of temperature.

It has been previously pointed out that PIH in Na-AlSi-NAT results in the formation of new hydrogen-bonded water nanotubes, which enclose sodium cations (Figs 2b and 3b)[9,10]. The PIH in K-GaSi-NAT, in contrast, leads to the formation of hydrogen-bonded water nanochains, which are retained at ambient conditions (Figs 2d and 3d); the hydrogen bonding between the water molecules at the OW3 site and those at the OW1 (or OW2) site generates a zigzag array of water molecules along the zeolitic channel (Fig. 3d). Unlike the water nanotubes in Na-AlSi-NAT, the water nanochains in K-GaSi-NAT have finite lengths because the water sites are not fully occupied (Supplementary Table 1). The different formation of water nanostructures after PIH can be related to the different arrangement of non-framework cations. At ambient conditions, potassium cations in K-GaSi-NAT occupy sites bound by the $T_{10}O_{20}$ windows close to the channel walls (Figs 2c and 3c) and water molecules are found along the channels (OW1 and OW2). This is the reverse of the sodium and water arrangements found in Na-AlSi-NAT (Figs 2a and 3a). The PIH in Na-AlSi-NAT does not cause any major redistribution of non-framework cations, whereas the potassium cations in K-GaSi-NAT are rearranged and merged into three closely separated sites away from the channel. The water nanochain in K-GaSi-NAT is thus surrounded by potassium cations (Figs 2d and 3d), whereas the water nanotube in Na-AlSi-NAT encloses sodium cations (Figs 2b and 3b). The migration and rearrangement of non-framework cations under pressure might have a crucial role in stabilizing the hydrogen-bonded water nanochains so that the PIH state in K-GaSi-NAT can be retained at ambient conditions but not that in Na-AlSi-NAT. As similar crystal chemical features occur in other zeolites and related framework materials, irreversible PIH and other unusual properties are likely to be observed in future work. Irreversible PIH, although at lower pressures, has the potential to immobilize tritiated water or other pollutant molecules. Furthermore, the expanded pore openings in the PIH state might markedly facilitate the ion exchange properties of these dense pore zeolites, which might then be used to trap radioactive ions by a subsequent pressure release ('trap-door' mechanism). □

Methods

In situ high-pressure experiments

The synthesis and crystal structure of K-GaSi-NAT were reported previously[11]. Variable-pressure powder diffraction data were measured with diamond anvil cells at beamline X7A of the National Synchrotron Light Source (NSLS). Each powdered sample was loaded into a 200-μm-diameter sample chamber in a pre-indented stainless steel gasket, along with a few small ruby chips as a pressure gauge. A methanol:ethanol:water mixture (16:3:1 by volume) was used as a pressure medium (hydrostatic up to ~10 GPa)[12]. The pressure at the sample was measured by detecting the shift in the R1 emission line of the included ruby chips. No evidence of non-hydrostatic conditions or pressure anisotropy was detected during our experiments, and the instrumental errors on the pressure measurements ranged between 0.05 and 0.1 GPa. Typically, the sample was equilibrated for ~15 min at each measured pressure, and diffraction data were collected for 3–5 h (3–35° 2θ, $\lambda = 0.6942(1)$ Å) using a micro-focused (~200 μm) monochromatic X-ray provided by a bent Si (220) monochromator and a gas-proportional position-sensitive detector[13]. The sample pressure was raised in 0.5–1.0 GPa increments before subsequent data measurements up to 5 GPa. There was no evidence of stress-induced peak broadening or pressure-induced amorphization. Several sets of diffraction data were measured after gradual pressure release. Unit-cell parameters were determined by whole-pattern fitting with the LeBail method. The diffraction peaks were modelled by varying only a half-width parameter in the pseudo-Voigt profile function. Bulk moduli were calculated by fitting the Murnaghan equation of state to normalized volumes ($V/V_0 = [1 + B'P/B_0]^{-1/B'}$, where $B' = (\partial B/\partial P)_{P=0} = 4$). The structural evolution of Na-AlSi-NAT was determined from the variable-pressure powder diffraction data and the Rietveld structure refinement[9,10].

Ex situ high-pressure experiments

Several needle-shaped crystals of K-GaSi-NAT were loaded into a diamond anvil cell as described above and initially pressurized at 1.9 GPa. After 2 weeks the sample pressure was measured as 1.3 GPa. The sample was subsequently recovered from the diamond anvil cell and kept at ambient conditions for 3 d before diffraction data measurement. A needle-shaped crystal of $5 \times 5 \times 50$ μm^3 was mounted on a glass fibre, and data collection was performed at ambient conditions at beamline X7B of the NSLS with an imaging plate detector (Mar345; 2,300 × 2,300 pixels). Diffraction data were measured in an oscillation mode by rotating the crystal in ϕ by 4° in 5 min per frame; 40 frames were measured. The intensities were integrated and merged with the DENZO program[14]. Corrections for Lorentz polarization effects were made, and no absorption correction was applied. The space group was determined by examining the systematic absences. Structural models were determined and refined with the SHELX program[15]. Refinements were based on full-matrix least-squares techniques on F^2. Anisotropic displacement factors were included for all framework atoms, whereas two sets of restrained isotropic displacement parameters were used for disordered non-framework cations and water molecules. The agreement factors for the final model were $R_1 = 0.0621$, $_wR_2 = 0.1462$, goodness of fit = 2.2 using 251 unique reflections with $I > 2\sigma$ ($R_{int} = 4.6\%$). The refinement results including atomic parameters and selected bond distances and angles are listed in Supplementary Information.

1. Breck, D. W. *Zeolite Molecular Sieves* (Krieger, Malabar, Florida, 1984).
2. Baur, W. H. & Joswig, W. The phases of natrolite occurring during dehydration and rehydration studied by single crystal x-ray diffraction methods between room temperature and 923K. *Neues Jb. Miner. Mh.* **4,** 171–187 (1996).
3. Miyamoto, T., Katada, N., Kim, J. H. & Niwa, M. Acidic property of MFI-type gallosilicate determined by temperature-programmed desorption of ammonia. *J. Phys. Chem. B* **102,** 6738–6745 (1998).
4. Lee, Y. *et al.* New insight into cation relocations within the pores of zeolite rho: In situ synchrotron X-ray and neutron powder diffraction studies of Pb- and Cd-exchanged rho. *J. Phys. Chem. B* **105,** 7188–7199 (2001).
5. Kuznicki, S. M. *et al.* A titanosilicate molecular sieve with adjustable pores for size-selective adsorption of molecules. *Nature* **412,** 720–724 (2001).
6. Hazen, R. M. Zeolite molecular-sieve 4A—anomalous compressibility and volume discontinuities at high-pressure. *Science* **219,** 1065–1067 (1983).
7. Belitsky, I. A., Fursenko, B. A., Gubada, S. P., Kholdeev, O. V. & Seryotkin, Y. V. Structural transformations in natrolite and edingtonite. *Phys. Chem. Minerals* **18,** 497–505 (1992).
8. Lee, Y. *et al.* Phase transition of zeolite rho at high-pressure. *J. Am. Chem. Soc.* **123,** 8418–8419 (2001).
9. Lee, Y., Hriljac, J. A., Vogt, T., Parise, J. B. & Artioli, G. First structural investigation of a super-hydrated zeolite. *J. Am. Chem. Soc.* **123,** 12732–12733 (2001).
10. Lee, Y., Vogt, T., Hriljac, J. A., Parise, J. B. & Artioli, G. Pressure-induced volume expansion of zeolites in the natrolite family. *J. Am. Chem. Soc.* **124,** 5466–5475 (2002).
11. Lee, Y., Kim, S. J. & Parise, J. B. Synthesis and crystal structures of gallium- and germanium-variants of the fibrous zeolites with the NAT, EDI and THO structure types. *Microporous Mesoporous Mater.* **34,** 255–271 (2000).
12. Hazen, R. M. & Finger, L. W. *Comparative Crystal Chemistry* (Wiley, New York, 1982).
13. Smith, G. C. X-ray imaging with gas proportional detectors. *Synch. Radiat. News* **4,** 24–30 (1991).
14. Otwinowski, Z. & Minor, W. Processing of X-ray diffraction data collected in oscillation mode. *Methods Enzymol.* **276,** 307–326 (1997).
15. Sheldrick, G. M. Phase annealing in SHELX90—direct methods for larger structures. *Acta Crystallogr. A* **46,** 467–473 (1990).

....

A short-term sink for atmospheric CO2 in subtropical mode water of the North Atlantic Ocean

Nicholas R. Bates*, **A. Christine Pequignet***, **Rodney J. Johnson*** & **Nicolas Gruber**†

* *Bermuda Biological Station For Research, Inc., Ferry Reach, Bermuda, GE01*
† *University of California at Los Angeles, Los Angeles, California 90095-4996, USA*

....

Large-scale features of ocean circulation, such as deep water formation in the northern North Atlantic Ocean[1], are known to regulate the long-term physical uptake of CO_2 from the atmosphere by moving CO_2-laden surface waters into the deep ocean. But the importance of CO_2 uptake into water masses that ventilate shallower ocean depths, such as subtropical mode waters[2] of the subtropical gyres, are poorly quantified. Here we report that, between 1988 and 2001, dissolved CO_2 concentrations in subtropical mode waters of the North Atlantic have increased at a rate twice that expected from these waters keeping in equilibrium with increasing atmospheric CO_2. This accounts for an extra $\sim$0.4–2.8 Pg C (1 Pg = 10^{15} g) over this period (that is, about 0.03–0.24 Pg C yr^{-1}), equivalent to $\sim$3–10% of the current net annual ocean uptake of CO_2 (ref. 3). We suggest that the lack of strong winter mixing events, to greater than 300 m in depth, in recent decades is responsible for this accumulation, which would otherwise disturb the mode water layer and liberate accumulated CO_2 back to the atmosphere. However, future climate variability (which influences subtropical mode water formation[1,4–8]) and changes in the North Atlantic Oscillation[9] (leading to a return of deep winter mixing events) may reduce CO_2 accumulation in subtropical mode waters. We therefore conclude that, although CO_2 uptake by subtropical mode waters in the North Atlantic—and possibly elsewhere—does not always represent a long-term CO_2 sink, the phenomenon is likely to contribute substantially to interannual variability in oceanic CO_2 uptake[3].

The net global ocean exchange of CO_2 between the ocean and the atmosphere depends on the rates of CO_2 flux across the air–sea interface, and the supply of CO_2 to (and its removal from) the ocean mixed layer. The transfer of CO_2 from the ocean mixed layer to deeper depths is a complex function of biological and physical processes that operate over a wide range of timescales ($<$1 to $>$1,000 yr). In subpolar/polar regions, the formation and subsequent sinking of intermediate and deep waters represent a physical mechanism for transporting CO_2 from the surface to the deep ocean. In the subtropical gyres, the shallow depths between the seasonal and main thermoclines are ventilated as a result of the formation of subtropical mode waters (STMWs)[2]. However, the

rates and interannual variability in the uptake of CO_2 from the atmosphere into STMW and the fate of this CO_2 are poorly quantified at present.

The STMW of the North Atlantic Ocean is formed each winter by cooling and convective mixing at the northern edges of the subtropical gyre south of the Gulf Stream[3–5]. The shallow depths of this gyre ($\sim$250–400 m)[4,10] are ventilated during STMW formation. The STMW layer is found throughout the subtropical gyre, and its age increases following the mean geostrophic circulation from the site of STMW formation to the western boundary current[11]. This water mass is classically defined by temperatures ranging from 17.8 to 18.4 °C (ref. 4), by a salinity of $\sim$36.5 $\pm$ 0.05, and by a minimum in the vertical gradient of potential density (or isopycnic potential vorticity)[2,5,7,12]. The strength and geographic extent of STMW formation is highly variable interannually[4,5,10,13], and primarily coupled to North Atlantic Oscillation (NAO)[1,4,5,8,13] variability— the NAO being a dipole meridional oscillation in atmospheric pressure between the Iceland Low and the Azores High[9]. Observations of STMW variability date back to 1954 with time-series hydrographic data collected at the Hydrostation S site (32° 10′ N, 64° 30′ W) near Bermuda[6,12–14], expendable bathythermograph (XBT) surveys since the 1960s[4,7], and monthly sampling since 1988 at the US Joint Global Ocean Flux Study (JGOFS) Bermuda Atlantic Time-series Study (BATS) site (31° 50′ N, 64° 10′ W) near Bermuda[15].
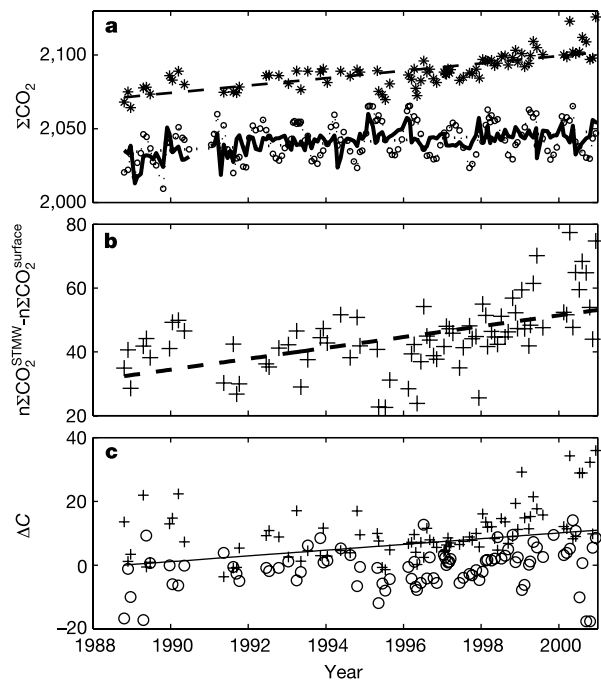

Figure 1 Interannual variability and trends of ΣCO_2 and hydrography in the western North Atlantic near Bermuda (1988–2001). **a**, Trends of surface ΣCO_2 (open circles) and STMW ΣCO_2 (asterisks) sampled at BATS from October 1988 to September 2001. Surface-layer ΣCO_2 data were normalized to the mean salinity of 36.6. Also shown are seasonally adjusted surface layer ΣCO_2 data, where the cyclo-stationary seasonal cycle has been removed by fitting harmonic functions of time with periods of 12, 6 and 4 months to the data. Regression lines are shown for the STMW layer (dashed line) and the surface layer (solid line). **b**, Difference between surface-layer and STMW ΣCO_2 sampled at BATS from October 1988 to September 2001. Both surface and STMW data have been adjusted to account for the cyclo-stationary seasonal cycle. The dashed line is the linear regression of the data. **c**, Long-term trends of C_{ant} (regression line), the gas exchange component C_{gasex} ('plus' symbols), and the biological component C_{bio} (open circles) in the STMW layer. Details and regression statistics are given in Table 1. $n\Sigma CO_2$, ΣCO_2 and ΔC units are µmol kg^{-1}.

489